Energy & Environmental Science

ROYAL SOCIETY OF CHEMISTRY

PAPER

View Article Online
View Journal | View Issue

Cite this: *Energy Environ. Sci.*, 2025, **18**, 7708

Non-linear spin correlation of intermediates in enhanced electrochemical nitrate reduction under magnetic fields†

Dongsheng Shao,‡[ab] Qian Wu,‡[b] Yuwei Zhang,‡[b] Xiyang Cai,[b] Chencheng Dai,[b] Siyuan Zhu,[b] Fanxu Meng,[b] Pengfei Song,[b] Xiaoning Li,[b] Xiaoming Ren,[a] Tianze Wu*[b] and Zhichuan J. Xu*[bc]

Received 17th April 2025,
Accepted 23rd June 2025

DOI: 10.1039/d5ee02132d

rsc.li/ees

Spin in electrocatalysis introduces a pivotal degree of freedom for overcoming thermodynamic and kinetic limitations. Paradigm studies on spin-related enhancement in oxygen electrocatalysis have highlighted the potential role of spin in influencing reaction kinetics. However, establishing spin correlations in reactions involving complex catalytic conversions, such as NH_3 synthesis, remains a significant challenge. Herein, we reveal spin correlations in electrochemical nitrate reduction (NO_3^-RR) by demonstrating enhanced activity under external magnetic fields. The yield rate enhancement under magnetic fields is demonstrated on magnetic $CuFe_2O_4$ at 93.2% for NH_3 production and more than one order of magnitude for NO_2^- production. Linear and non-linear correlations between the activity enhancement and spin polarization improvement of $CuFe_2O_4$ are revealed for NO_3^-RR toward NO_2^- and NH_3, respectively. Insights into spin polarization are provided on intermediates with different net spins, which facilitates the development of magnetic electrocatalysts for NO_3^-RR.

Broader context

Spin effects in electrocatalysis have shown great potential for overcoming kinetic and energetic limitations in a range of reactions. Notably, studies have demonstrated that spin-related phenomena can enhance the performance of ferromagnetic catalysts, particularly in oxygen electrocatalysis, where activity improvements are observed under applied magnetic fields. However, NH_3 synthesis, especially *via* electrochemical nitrate reduction, involves a much more complicated elementary reaction than oxygen electrocatalysis, which prevents spin effects from being revealed in a straightforward way. In this study, beyond the observed enhancement of NO_3^-RR using ferromagnetic catalysts under magnetic fields, the improvements are associated with the net spin of the intermediates. The improvements are correlated with the net spins of reaction intermediates. Due to the diverse spin configurations of these intermediates, the relationship between catalytic enhancement and the degree of ferromagnetic ordering becomes non-linear and more intricate.

Introduction

Electrocatalysis plays a pivotal role in the sustainable use of renewable energy.[1–6] The development of efficient electrocatalysts depends on a deep understanding of the relationship between their electrocatalytic activity and electronic structure. Structure–activity relationships have been established based on relevant descriptors such as the d-band center, e_g occupancy, O 2p band energy, metal–oxygen covalency, valence state of the active site, charge-transfer energy and the number of d electrons.[3,7–11] Typically, electrocatalytic activity is regulated according to these descriptors to achieve optimal adsorption/desorption energetics of intermediates.[7,8] However, considering only the energetics of intermediates can maintain the limitations in the reaction kinetics. For instance, in oxygen electrocatalysis, *OH, *O, and *OOH intermediates can scale adsorption energies, introducing an energy barrier that is difficult to overcome.[12,13] In addition, electrochemical reactions can be limited by significant kinetic barriers, primarily caused by the high activation energy required for the conversion of intermediates.

[a] State Key Laboratory of Materials-Oriented Chemical Engineering and College of Chemistry and Molecular Engineering, Nanjing Tech University, Nanjing 211816, China
[b] School of Materials Science and Engineering, Nanyang Technological University, 50 Nanyang Avenue, Singapore 639798, Singapore. E-mail: tianze.wu@ntu.edu.sg, xuzc@ntu.edu.sg
[c] The Centre of Advanced Catalysis Science and Technology, Nanyang Technological University, 50 Nanyang Avenue, Singapore 639798, Singapore

† Electronic supplementary information (ESI) available. See DOI: https://doi.org/10.1039/d5ee02132d

‡ These authors contributed equally to this work.

Spin manipulation for catalysts potentially introduces an additional degree of freedom to overcome the scaling relationships for intermediates and the activation energy among intermediates with different spin-multiplicity.[14–16] The crucial roles of spin have been demonstrated in the reaction kinetics of oxygen electrocatalysis.[14–19] For example, in some DFT studies, the binding energy of reaction intermediates is regulated by open–shell quantum spin exchange interactions (QSEI), leading to higher catalytic activity with ferromagnetic (FM) coupling compared to that with antiferromagnetic (AFM) coupling.[20,21] This potentially bypasses the energy scaling between key intermediates and could lead to spin-related reaction pathways with more favourable energetics and kinetics.

Approaches to control electron spins include the manipulation of chirality and magnetic ordering of catalysts.[15–19,22–25] Chirality-induced spin selectivity (CISS) effect describes the preferential transmission of electrons with a specific spin orientation through chiral molecules, effectively enabling them to function as spin filters. Zhang *et al.* synthesized chiral nanostructured Ag films and observed a pronounced improvement in faradaic efficiency (FE) for C_2^+ products compared with racemic and achiral ones in the electrochemical CO_2 reduction reaction.[24] Other than molecular strategies, spin regulation can also be assisted by magnetic ordering of catalysts under an external magnetic field. Pioneering studies on the OER revealed that magnetizing ferromagnetic (FM) catalysts enhances current density under magnetic fields.[17–19]

To realize effective spin regulation in catalysis, it is essential to establish the relationship between spin polarization and catalytic performance. Magnetic field-regulated oxygen evolution reaction (OER) has been investigated as a model system for exploring possible spin-related effects in catalysis (Fig. 1(a) and (b)).[14,15,17–19] In FM catalysts, magnetization eliminates the domain wall region to evolve a single-domain state, which promotes the spin polarization of catalysts (Fig. 1(c)).[19] In these cases, the OER enhancement showed a linear relationship with the degree of spin polarization. This linear relationship is based on a straightforward association between the O–O coupling efficiency and the spin polarization of intermediate oxygen radicals on the catalysts, which is typically rate-determining in OER (Fig. 1(b)).[18] However, complicated spin correlations will provide more spin-related insights into the reaction kinetics of complex catalytic systems to extend the study of spin electrocatalysis. Recent progress for Haber–Bosch ammonia synthesis has demonstrated that spin-mediated promotion activates traditionally unreactive magnetic materials

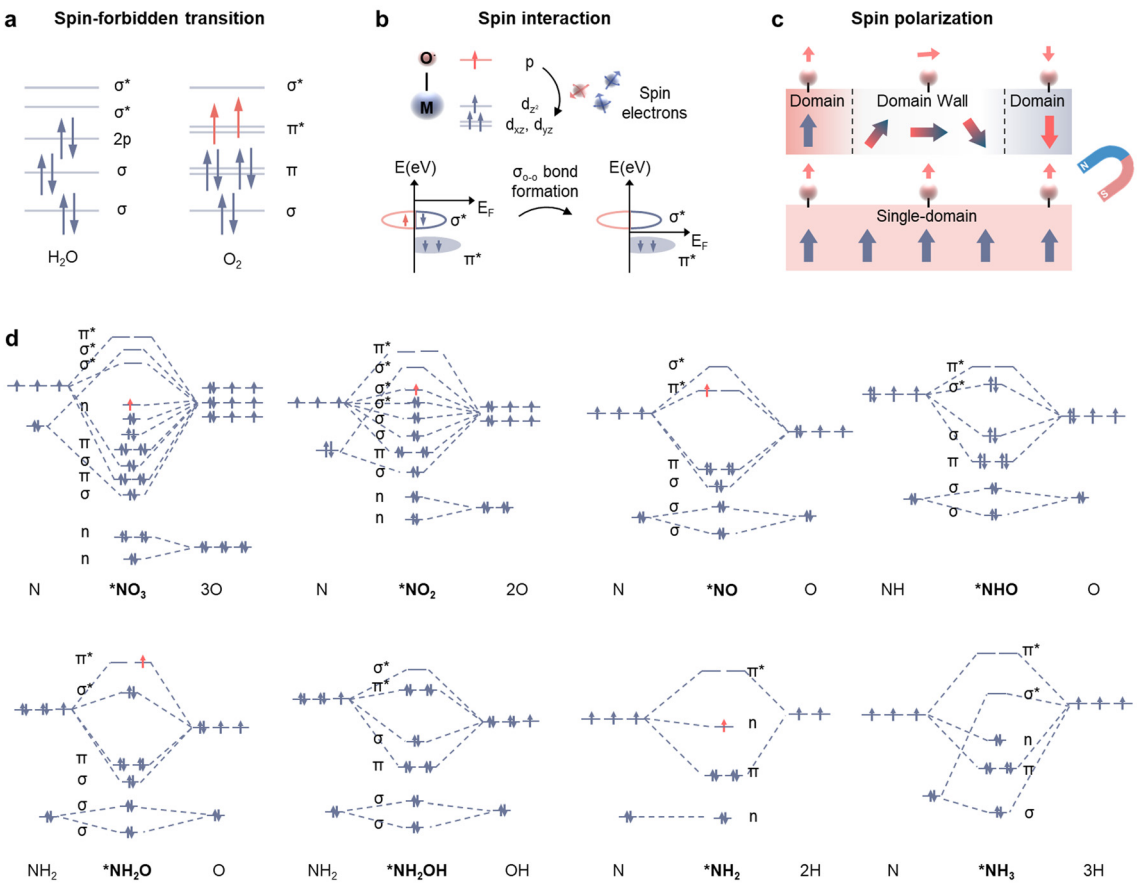

Fig. 1 Potential spin effect in NO_3^-RR. (a) Schematic of the conversion of H_2O to O_2 involving a change in spins, which is forbidden. (b) Scheme of O–O coupling and triplet O_2 turnover process with spins aligned in the nearest M–O radicals. (c) Schematic of the evolution of the magnetization-induced FM catalyst from a multi-domain to a single domain. (d) Molecular orbitals of possible intermediates.

such as cobalt, suggesting an interesting role of spin in NH_3 synthesis.[26] As one of the methods for the electrochemical synthesis of NH_3, NO_3^-RR involves eight electron transfer steps ($NO_3^- + 6H_2O + 8e^- \rightarrow NH_3 + 9OH^-$),[27–30] featuring complicated reaction intermediates including $*NO_3$, $*NO_2$, *NO, *NHO, $*NH_2O$, $*NH_2OH$, *NH and $*NH_3$.[31–35] In the pathway for NO_3^-RR, the net spins in these intermediates frequently change (Fig. 1(d)),[36–39] which calls for the spin regulation in relevant elementary steps.

In this study, we showcase the complicated spin correlations in NO_3^-RR by demonstrating activity enhancement under magnetic fields. Model catalysts, including Cu, Fe_3O_4, and $CuFe_2O_4$, were examined for NO_3^-RR under magnetic field conditions. While the NH_3 yield rates and FE of Cu foil in the NO_3^-RR process show negligible changes upon the application of a magnetic field, the magnetic catalysts Fe_3O_4 and $CuFe_2O_4$ exhibit significant NO_3^-RR enhancements. The NH_3 yield rate and FE enhancement for $CuFe_2O_4$ reached 93.2% and 30.3%, respectively, at −1.1 V *vs.* RHE. Notably, an activity enhancement for NO_2^- production achieves more than one order of magnitude. The activity enhancement shows linear and nonlinear correlations for NO_2^- and NH_3 production, respectively. Such a difference originates from the varied response of the elemental electron transfer step to magnetization according to the magnetic nature of key intermediates, as revealed by DFT simulation. This study presents essential fundamentals for NO_3^-RR electrocatalyst optimization by spin manipulation and maximizing the practical potential of employing a magnetic field to elevate the intrinsic NO_3^-RR activity.

Results and discussions

Spin-promoted NO_3^-RR under a magnetic field condition

The magnetic $CuFe_2O_4$ (spinel oxide) was prepared by a conventional sol–gel method as previously reported.[40] The powder X-ray diffraction (XRD) pattern confirms the crystal structure. The pattern is consistent with that of the standard tetragonal spinel (*I*41/*amd*), indicating the high phase purity of the catalyst (Fig. S1, ESI†). Field emission scanning electron microscopy (FESEM) images of $CuFe_2O_4$ catalyst at different scales and the distribution of Cu, Fe, and O elements are shown in Fig. S2 and S3 (ESI†). The prepared sample nanoparticles have irregular shapes with a size of approximately 100 nm. Elemental mapping images and atom percentage analysis revealed that Cu, Fe, and O were homogeneously distributed. The magnetic properties of the employed catalysts, Cu foil, Fe_3O_4, and $CuFe_2O_4$, were investigated using a vibrating sample magnetometer (VSM) at room temperature. The MH curves for the employed catalysts were tested in the magnetic field range from −14 to +14 kOe, and are shown in Fig. 2(a). Cu foil exhibited typical diamagnetic behavior, whereas Fe_3O_4 and $CuFe_2O_4$ exhibited S-shaped hysteresis loops with a coercive field, indicating ferromagnetic behavior. The coercive field, which measures a

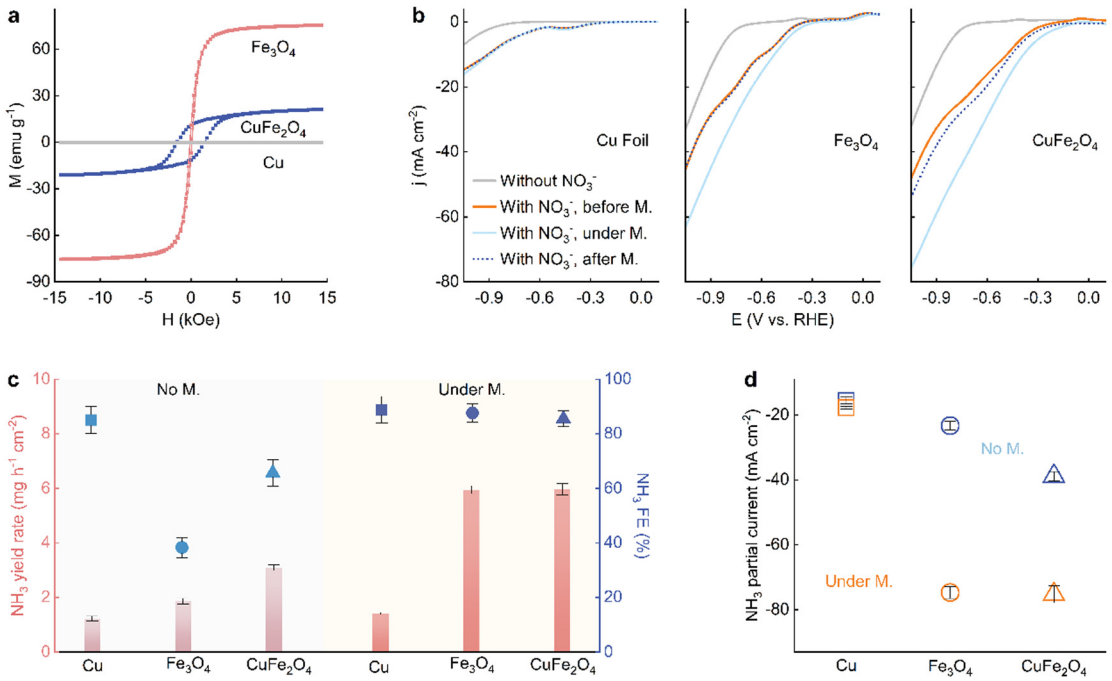

Fig. 2 Magnetic field-enhanced NO_3^-RR on ferromagnetic catalysts. (a) Magnetic hysteresis loops of Cu foil, Fe_3O_4, and $CuFe_2O_4$ at room temperature. (b) Steady-state linear sweep voltammetry (LSV) curves of Cu foil, Fe_3O_4, and $CuFe_2O_4$ catalysts at a scan rate of 10 mV s^{-1} in Ar-saturated electrolyte (0.5 M Na_2SO_4 and 0.5 M Na_2SO_4 + 0.1 M $NaNO_3$) with and without an external magnetic field of 2500 Oe. (c) Comparison of NH_3 yield rate and NH_3 FE of Cu foil, Fe_3O_4, and $CuFe_2O_4$ with and without an external magnetic field of 2500 Oe at −1.1 V *vs.* RHE. Error bars represent the standard deviations of three independent measurements, with the center value indicating the average of these three independent measurements. (d) Comparison of the NH_3 partial current of Cu foil, Fe_3O_4, and $CuFe_2O_4$ with and without an external magnetic field of 2500 Oe at −1.1 V *vs.* RHE.

material's resistance to demagnetization, was small for Fe_3O_4 at 107.8 Oe but significantly larger for $CuFe_2O_4$ at 1519.7 Oe.

The NO_3^-RR performance of the Cu foil, Fe_3O_4, and $CuFe_2O_4$ was investigated in a 0.5 M Na_2SO_4 electrolyte with 0.1 M $NaNO_3$ at room temperature in an optimized setup (Fig. S4, see Methods for details). As shown in linear sweep voltammetry (LSV) curves of the catalysts in Fig. 2(b), the current density (j) of all catalysts shows an obvious increment after adding 0.1 M $NaNO_3$. Furthermore, the NO_3^-RR performance of the ferromagnetic Fe_3O_4 and $CuFe_2O_4$ is significantly enhanced under an external magnetic field of 2500 Oe, while the changes in the nonmagnetic catalyst Cu foil are negligible. Once the magnetic field was removed, the improved NO_3^-RR activity of ferromagnetic Fe_3O_4 promptly reverted nearly to its unmagnetized state, whereas the activity of $CuFe_2O_4$ after removing the magnetic field still exceeds the one before magnetization. This is attributed to the higher coercivity of $CuFe_2O_4$ than that of Fe_3O_4, which contributes to the maintenance of the spin polarization in materials after magnetization.

Chronoamperometry (CA) measurements were carried out at a constant potential of −1.1 V *vs.* RHE for 0.5 h, after which the NH_3 concentration was measured by ultraviolet-visible (UV-Vis) spectrophotometry (Fig. S5, ESI;† see Methods for details). As shown in Fig. 2(c), the NH_3 yield rate follows the order Cu foil < Fe_3O_4 < $CuFe_2O_4$ without an applied magnetic field. When an external magnetic field of 2500 Oe was applied, the NH_3 yield rate and FE of the nonmagnetic Cu foil catalyst showed negligible improvement at −1.1 V *vs.* RHE. In contrast, for Fe_3O_4, the NH_3 yield rate increased from 1.9 ± 0.1 to 6.0 ± 0.2 mg h^{-1} cm^{-2} (a 3.2-fold increase), and the FE improved from 38.3 ± 3.7% to 87.6 ± 3.4% (a 2.3-fold increase) under a 2500 Oe magnetic field. The corresponding NH_3 partial current density increased from −23.3 to −74.7 mA cm^{-2} (Fig. 2(d)). Similarly, for $CuFe_2O_4$, the NH_3 yield rate increased from 3.1 ± 0.1 to 6.0 ± 0.2 mg h^{-1} cm^{-2} (a 1.9-fold increase), and FE increased from 65.6 ± 4.8% to 85.5 ± 2.9% (a 1.3-fold increase), with the NH_3 partial current density rising from −38.9 to −75.3 mA cm^{-2} (Fig. 2(d)). To exclude the effects of magnetic fields on the mass transport, such as Lorentzian movement,[17] we measured the NH_3 produced by Cu foil with and without a magnetic field under different potentials (Fig. S6, ESI†) and found a negligible improvement in NH_3 production. This evidence excludes the mass transport effects as a major contributor to the significant NO_3^-RR enhancement under the magnetic field. To exclude the influence of the substrate electrode, we tested the NO_3^-RR performance of a bare carbon paper electrode, which showed negligible nitrate reduction activity to NH_3 with and without an external magnetic field (Fig. S7, ESI†). In addition, we excluded the influence of magnetic fields on the electrochemical surface area (ECSA) of catalysts (Fig. S8 and S9, ESI†). However, the ECSA-normalized NO_3^-RR activity still exhibited activity enhancement under the magnetic field (Fig. S10, ESI†).

CA measurements were conducted for Fe_3O_4 and $CuFe_2O_4$ at different potentials with and without an external magnetic field of 2500 Oe. The NH_3 yield rate and FE are shown as a function of applied potentials in Fig. 3(a) and Fig. S6 (ESI†). The significant activity enhancement for $CuFe_2O_4$ is found at potentials of −1.1 V and −0.9 V *vs.* RHE, while as the potential decreased to −0.7 V *vs.* RHE, the performance improvement is weakened and becomes minimal at −0.5 V and −0.3 V *vs.* RHE. The FE for NH_3 in NO_3^-RR system is typically below 100%, primarily due to competing side reactions and minor NO_3^-RR byproducts, including NO_2^- and potentially trace nitrogen-containing species. We quantify both NH_3 and NO_2^- faradaic efficiencies with and without an external magnetic field across a range of potentials to clarify the origin of the FE deficit (Fig. S11, ESI†).

During NO_3^-RR, the effects of the magnetic field demonstrate profound scientific implications during the studies of elemental reactions (*e.g.*, $NO_3^- \rightarrow NO_2^-$, $NO_2^- \rightarrow NH_3$). Nitrite ion (NO_2^-) is an important intermediate by-product during NO_3^-RR, and its yield rate and selectivity under magnetic fields are screened along with the applied potentials (Fig. 3(b) and Fig. S12, ESI†). Under an applied magnetic field of 2500 Oe, the yield rate of NO_2^- increased significantly at nearly all potentials. Maximal enhancement was found at −0.7 V *vs.* RHE, with the yield rate of NO_2^- increased from 0.26 to 7.13 mg h^{-1} cm^{-2}, which represents a remarkable enhancement by more than one order of magnitude. Similarly, the NH_3 and NO_2^- partial current density for $CuFe_2O_4$ increased significantly under a magnetic field of 2500 Oe (Fig. 3(c)).

NO_2^- is an intermediate byproduct that is further converted to NH_3. We performed NO_2^- reduction reaction (NO_2^-RR) on $CuFe_2O_4$ with and without a magnetic field. As shown in Fig. S13 (ESI†), $CuFe_2O_4$ exhibited the highest performance for NO_2^-RR at −1.1 V *vs.* RHE. After a 2500 Oe magnetic field was applied, the NH_3 yield rate increased from 3.35 mg h^{-1} cm^{-2} to 6.99 mg h^{-1} cm^{-2}, and FE increased from 51.7% to 79.0% respectively, demonstrating a significant promotion due to the magnetic field.

Furthermore, we analyzed NH_3 produced from ^{15}N isotope-labeled NO_3^- using ^1H nuclear magnetic resonance (NMR) analysis (Fig. 3(d)). Only two peaks of $^{15}NH_4^+$ appeared in the ^1H NMR spectra, and their peak intensity approximately doubled under the magnetic field, confirming the promoted NH_3 production directly sourced from NO_3^-. The durability of $CuFe_2O_4$ in NO_3^-RR was evaluated through 14 consecutive CA measurements, with the magnetic field (2500 Oe) repeatedly applied or removed. The NH_3 yield rate and FE were analyzed 1 h after each session (Fig. 3(e)). Please note that after each session, the electrolyte was completely collected and refilled with a new electrolyte. We did not find notable activity differences due to the replacement of electrolytes (Fig. S14, ESI†). As shown in Fig. 3(e), the NH_3 yield rate and FE in each segment show negligible difference, indicating the high repeatability of NO_3^-RR improvement by applying magnetic fields and its durable electrochemical performance. After the CA tests, the high-resolution transmission electron microscope (HRTEM, Fig. S15, ESI†), FESEM images (Fig. S16a and b, ESI†), and elemental mapping images (Fig. S16c–f, ESI†) showed that the structure and morphology of the $CuFe_2O_4$ catalyst remained

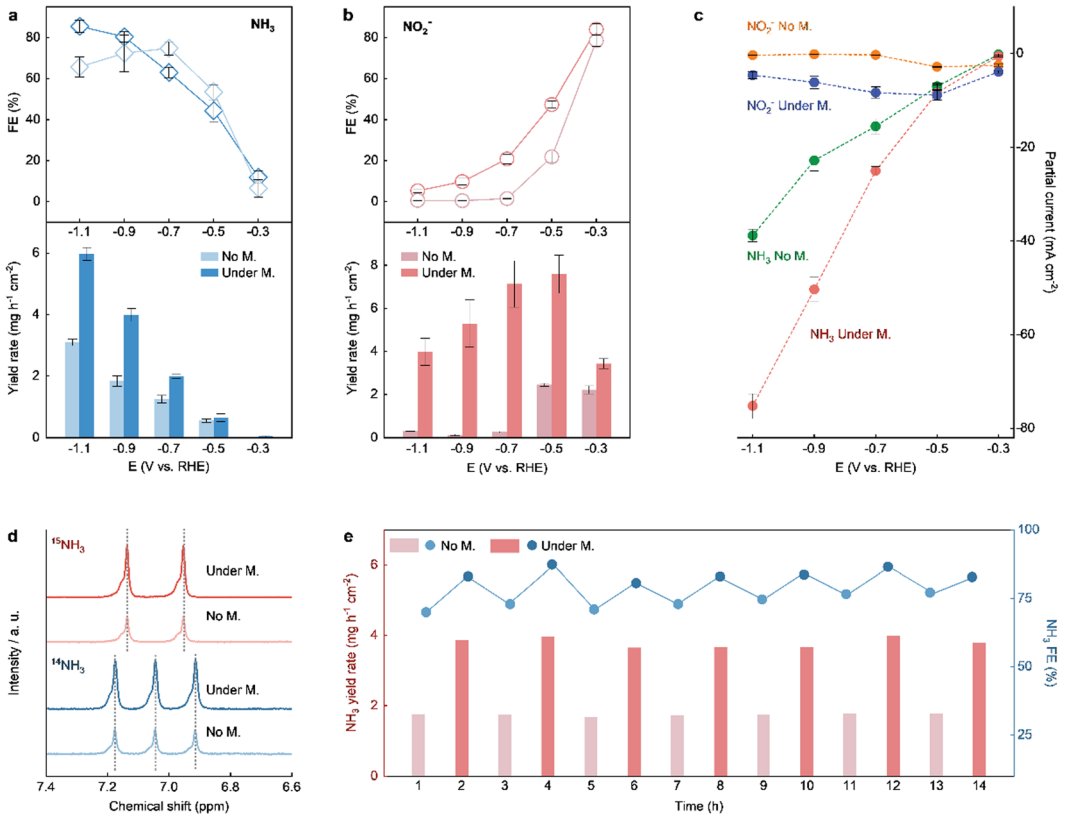

Fig. 3 Influence of an external magnetic field on NO_3^-RR performance. (a)–(c) NH_3 yield rate and NH_3 FE (a), NO_2^- yield rate and NO_2^- FE (b), and NH_3 partial current and NO_2^- partial current (c) of $CuFe_2O_4$ with and without an external magnetic field of 2500 Oe at various applied potentials. (d) ^{1}H NMR spectra of the products generated after electrocatalysis on $CuFe_2O_4$ with and without an external magnetic field of 2500 Oe at −1.1 V *vs.* RHE, using 0.1 M $Na^{15}NO_3$ or 0.1 M $Na^{14}NO_3$ in 0.5 M Na_2SO_4 as the nitrogen source. (e) NH_3 yield rate and FE of $CuFe_2O_4$ at −0.9 V *vs.* RHE during 14 consecutive CA measurements (1 h per section), during which we repeatedly applied and removed the external magnetic field.

nearly identical to that before the electrochemical test, indicating the material stability of $CuFe_2O_4$ during NO_3^-RR.

Catalyst chemistry after NO_3^-RR

The catalyst chemistry during NO_3^-RR is studied by post-electrochemistry analyses and operando characterizations. The powder XRD pattern of $CuFe_2O_4$ showed negligible change after 1 h of CA tests in 0.5 M Na_2SO_4 + 0.1 M $NaNO_3$ (Fig. S17, ESI†). The operando Raman tests were performed under different applied potentials to track the structural change at a smaller scale. As shown in Fig. S18 (ESI†), $CuFe_2O_4$ displays several Raman active modes of E_g (446 cm^{-1}), B_{1g} (491 cm^{-1} and 571^{-1}), and A_{1g} (706 cm^{-1}). A_{1g} is identified as symmetric stretching of metal–oxygen bonds in tetrahedral sites. The other E_g and B_g modes are assigned to metal ions in octahedral sites.[41,42] In addition, the vibrational bands of 980 cm^{-1} and 1047 cm^{-1} can be assigned to adsorbed SO_4^{2-} and NO_3^-, respectively. As the applied potential shifts from −0.1 to −1.1 V *vs.* RHE, almost no change in the vibrational modes was observed. HRTEM before and after NO_3^-RR proved that the $CuFe_2O_4$ crystal structure was well maintained (Fig. S19, ESI†).

As shown in Fig. S20 and S21 (ESI†), X-ray photoelectron spectrum (XPS), and Auger electron spectroscopy (AES) tests were performed on $CuFe_2O_4$ after electrochemical measurements. In Cu 2p XPS spectra, the peak located at 934.4 eV in $CuFe_2O_4$ is assigned to Cu^{2+}, while an additional small peak at 932.5 eV is assigned to Cu^0 after nitrate electrochemical reduction.[43,44] The Auger peaks of Cu^0 and Cu^{2+} were observed at 568 and 568.9 eV,[45] respectively, and a small peak for Cu^0 emerges after NO_3^-RR. The peaks at 711.0 and 724.4 eV in the Fe 2p XPS spectra can be attributed to Fe^{3+} in the octahedral sites, and the peaks at 713.6 and 726.9 eV can be attributed to Fe^{3+} in the tetrahedral sites. The O 1s spectra have three main peaks at 530.5, 532.1, and 535.3 eV, which can be attributed to bulk lattice oxygen ($O_{lattice}$), surface oxygen ($O_{surface}$), and adsorbed oxygen (O_{absorb}). These peaks remained unchanged in location before and after the NO_3^-RR.

The valence state and the density of partially/empty filled electronic states of $CuFe_2O_4$ were further revealed by soft X-ray absorption spectroscopy (SXAS) at the Cu 2p, Fe 2p, and O 1s edges (Fig. S22, ESI†) before and after NO_3^-RR. The dipole transitions of Cu 2p3/2 and 2p1/2 electrons into empty d-states are illustrated in the Cu L-edge XAS spectrum.[46,47] In Cu L-edge XAS spectra, the peaks at 930.6 and 950.6 eV in $CuFe_2O_4$ are assigned to Cu^{2+}, corresponding to the transitions of Cu 2p3/2 and Cu 2p1/2 (spin–orbital coupled states) to the $3d^9$ unoccupied orbital, respectively. A small peak at 939.9 eV appears after NO_3^-RR, which can be attributed to Cu^0. This finding is

consistent with the XPS and AES results, confirming that a small amount of Cu^{2+} was reduced to Cu^0. In the Fe L-edge XAS spectra, four intense peaks at 708/709.4 eV and 721.2/722.8 eV are assigned to the Fe 2p3/2 and Fe 2p1/2, respectively.[46] Compared to the Fe L-edge XAS spectra of $CuFe_2O_4$ before the NO_3^-RR, the peaks remained unchanged after the NO_3^-RR. Furthermore, the O K-edge XAS spectra of $CuFe_2O_4$ had five peaks, which were resolved at 530, 531, 537.4, 540.6, and 546.5 eV, respectively. The peaks at 530 and 531 eV are assigned to O 1s and O p orbitals hybridized with metal 3d orbitals, and the other three peaks are assigned to O 1s and O p orbitals hybridized with metal 4s and 4p orbitals.[46] Slight changes in peak intensity after NO_3^-RR suggest a small amount of Cu^{2+} was reduced, altering the metal-oxygen hybridization. Overall, $CuFe_2O_4$ is the main catalytic motif for the spin-sensitive NO_3^-RR process. Although minor Cu^0 segregation was identified on the $CuFe_2O_4$ surface, the Cu foil experiment excluded the contribution of Cu^0 to the enhanced NO_3^-RR under magnetic fields. Our subsequent theoretical study was conducted using $CuFe_2O_4$ as the simulation model.

Insights into spin-polarized NO_3^-RR

To investigate the reaction mechanism of NO_3^-RR on $CuFe_2O_4$, *in situ* ATR-FTIR tests were performed to detect the key absorbed intermediates and products during NO_3^-RR (Fig. 4(a) and Fig. S23, ESI†). In the potential-dependent and time-dependent *in situ* ATR-FTIR spectra, a series of characteristic peaks associated with NO_3^-RR intermediates gradually intensified as the applied potential became more negative and the reaction progressed. Notably, the bands at 1456 cm^{-1} and 1228 cm^{-1} correspond to the N–H bending vibration of $*NH_3$ species[48–50] and the N–O stretching vibration of $*NO_2$, respectively.[49,51] Their gradual intensification indicates an enhancement in the reaction, which is consistent with the results of the electrochemical testing. In addition, several weaker but distinguishable peaks emerged, reflecting the presence of multiple intermediates: the N=O scaling vibration of *NHO (1397 cm^{-1}),[48] the antisymmetric N–H bending of $*NH_2$ (1538 cm^{-1}),[48,49] the N–O stretching vibration of $*NO_3^-$ (1338 cm^{-1}),[48,49] the N–O bending vibration in *NO (1611 cm^{-1}),[49,50,52] and the N–O stretching of hydroxylamine $*NH_2OH$ (1153 cm^{-1}).[50,52] The gradual enhancement of these characteristic peaks indicates an intensifying reaction that is consistent with electrochemical testing observations. Based on the *in situ* ATR-FTIR results, the NO_3^-RR could proceed through the $* + NO_3^- \rightarrow *NO_3 \rightarrow *NO_2 \rightarrow *NO \rightarrow *NHO \rightarrow *NHOH$ or $*NH_2O \rightarrow *NH_2OH \rightarrow *NH_2 \rightarrow *NH_3$ pathways. Either with *NHOH or $*NH_2O$ intermediate will decide for alternative pathways, which were both studied by spin-polarized density functional theory to identify the favorable pathway. A low-index (110) surface was used to model the adsorption of the intermediates on the spinel $CuFe_2O_4$ surface, and a 1 × 2 supercell was constructed. As shown in Fig. S24 (ESI†), $*NO_3$ is preferably adsorbed on Fe atoms rather than Cu atoms; thus, Fe could serve as the main site for subsequent

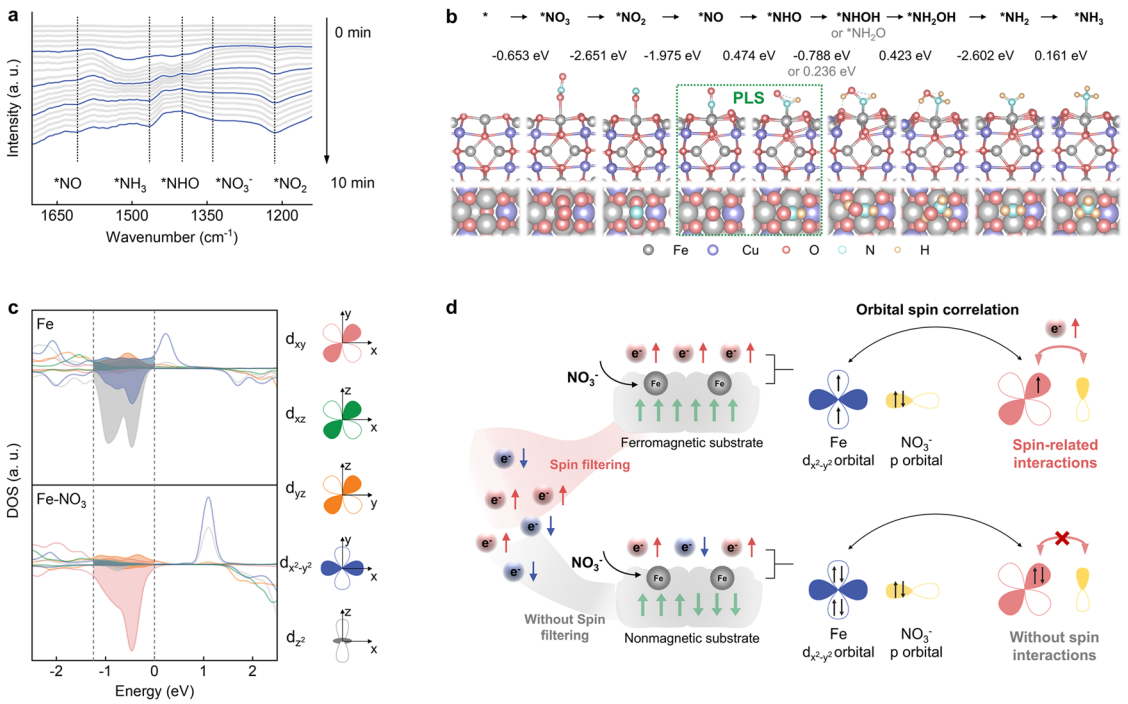

Fig. 4 Insights into spin-polarization in NO_3^-RR. (a) *In situ* ATR-FTIR spectra of $CuFe_2O_4$ at −0.7 V *vs.* RHE from 0 to 10 minutes in 0.5 M Na_2SO_4 + 0.1 M $NaNO_3$. (b) Change in free energy of intermediates on $CuFe_2O_4$ and the computational models of reaction intermediates absorbed on the Fe site of $CuFe_2O_4$, along with NO_3^-RR reaction coordinates. (c) DOSs of the Fe atom on $CuFe_2O_4$ before and after $*NO_3$ adsorption, and spatial illustration of the five Fe d-orbitals and three d-orbitals. (d) Schematic mechanism of electron transfer between active sites and $*NO_3$, showing the transfer modes of the polarized and paired electrons.

hydrogenation and deoxygenation processes. The free energy diagram of all reaction intermediates on $CuFe_2O_4$ is shown in Fig. S25 (ESI†), and the corresponding intermediate configurations are summarized in Fig. 4(b). As displayed, the NO_3^- adsorption step, $* + NO_3^- \rightarrow *NO_3 + e^-$, shows a downhill Gibbs free energy change of −0.653 eV. Subsequently, $*NO_3$ undergoes two deoxygenation steps to become *NO with a downhill free energy change of −2.651 eV and −1.975 eV, respectively. Therefore, the two steps of NO_3^- deoxygenated to *NO on $CuFe_2O_4$ are thermodynamically favorable. The potential limiting step (PLS) is found in the first hydrogenation step from *NO to *NHO with a limiting potential of 0.474 eV. The hydrogenation of *NHO could result in either $*NH_2O$ or *NHOH, whereas the formation of *NHOH is energetically more favorable. In addition, the free energy diagram of NO_2^-RR on $CuFe_2O_4$ is shown in Fig. S26 (ESI†); the only difference from NO_3^-RR is the adsorption of NO_2^- in the first reaction step. The diagram indicates that the free energy changes from $*NO_2$ to $*NH_3$ in NO_2^-RR are consistent with those observed in NO_3^-RR, with the PLS also being the conversion of *NO to *NHO.

To explain the improvement by magnetization, we employ DFT studies to reveal the spin-related interactions among reaction intermediates and identify the spin effects on the PLS. The d-band density of states (DOSs) for the Fe sites of $CuFe_2O_4$ were calculated, and the results are shown in Fig. 4(c). The Fe 3d spin-up and spin-down states around the Fermi level (E_F) are asymmetric about the *x*-axis, indicating that the unpaired electrons belong to the 3d orbitals. Fe was calculated using a spin population of $3.526\mu_B$. Similarly, according to the DOSs of all NO_3^-RR intermediates (Fig. S27, ESI†), significant spin density is identified for the atoms (N or O) directly associated with Fe. The corresponding electronic interactions within these reaction intermediates are crucial for leading spin-polarized pathways.

Subsequently, we studied the DOS (Fig. 4(c) and Fig. S28, ESI†) of the Fe of $CuFe_2O_4$ before and after the adsorption of the intermediates, revealing changes in the electronic structure of the orbitals. After the adsorption of $*NO_3$, new occupied electronic states appear in the Fe d_{xy} orbital near the Fermi level, whereas the occupied states of the Fe $d_{x^2-y^2}$ and d_{z^2} orbitals disappear. Notably, the spin direction of the filled electrons in the d_{xy} orbital after adsorption is consistent with that in the Fe $d_{x^2-y^2}$ and d_{z^2} orbitals before adsorption. Such association by spin direction is schematically illustrated in Fig. 4(d) to indicate the role of ferromagnetism in reaction kinetics. When a ferromagnetic substrate is magnetized, spin polarization in the materials facilitates spin filtering. During electrochemical reduction, the electrons passing through the electrode are aligned by the magnetized substrate to the same spin direction. The spin electron transfer, mediated by Fe $d_{x^2-y^2}$ and d_{z^2} orbitals, induces significant spin-polarized electrons in the Fe d_{xy} orbital, which results in the π interactions between Fe d_{xy} and N or O p orbitals of adsorbed nitrogenous species to be spin-correlated. In the absence of spin filtering by a magnetized substrate or using inherently non-ferromagnetic catalysts, significantly disordered spins can dominate Fe $d_{x^2-y^2}$ and d_{z^2}, leading to electron pairing in the d_{xy} orbital without spin interactions with the adsorbed species. Therefore, in terms of orbital-level spin interactions, the ferromagnetic spin ordering of electrocatalysts could be a prerequisite for the spin polarization of intermediates during NO_3^-RR.

The correlation between activity enhancement and the degree of spin polarization in electrocatalysts is important for understanding the performance improvement mechanism. In a past study, a linear correlation for OER enhancement as a function of spin polarization degree was indicated by the portion of disappeared domain walls after NiFe thin films were magnetized.[29] In this study, we achieved varying degrees of spin polarization in $CuFe_2O_4$ by gradually increasing the magnetic field from zero to magnetic saturation (2500 Oe according to the hysteresis loop of $CuFe_2O_4$ in Fig. S29, ESI†). The inset in Fig. 5(a) shows the increment in current density corresponding to the magnetic field strength, ranging from 0 to 2500 Oe. A product analysis was conducted after a series of CA measurements (−1.1 V *vs.* RHE, 0.5 h) under elevating magnetic fields. Tables S2 and S3 (ESI†) summarize the yield rate and FE for both NH_3 and NO_2^- under varying magnetic fields, respectively. Fig. 5(a) plots the yield rate increment for NH_3 and NO_2^- as a function of the magnetic field strength. For NH_3, the yield rate increment exhibits a nearly linear correlation with the magnetic field strength up to 1000 Oe. However, once magnetic field strength exceeded 1000 Oe, the effect on NH_3 yield rate increment plateaus, disrupting the linear relationship with spin polarization. In contrast, the yield rate increment for NO_2^- maintains a linear correlation with the magnetic field strength throughout the field range. The dependence of the reaction kinetics on spin polarization shows a striking difference between the production of NO_2^- and NH_3, implying that spin has distinct roles in their respective reaction pathways.

The magnetic moments of Fe and adsorbed intermediates were calculated along with the NO_3^-RR pathway and are summarized in Fig. 5(b). These calculations reveal dynamic variations in the magnetic moments during deoxygenation and hydrogenation processes. Upon the formation of $*NO_3$, both the Fe atoms and the adsorbed intermediates exhibit increasing magnetic moments. Significant magnetic moments were identified for the *NO and *NHO intermediates. The transition to these intermediates requires substantial spin polarization, making the relevant electrochemical step highly sensitive to the magnetization of the electrocatalyst. As electrons pass through the magnetized catalyst, they are more likely to be filtered into the same spin direction, enhancing the spin polarization in the reaction.

The step of *NO → *NHO is spin-sensitive and coincides with PLS. Tuning it by improving the spin-polarization of the catalyst has a high likelihood of promoting the reaction kinetics. Upon the formation of *NHO, Fe reaches its maximal magnetic moment ($3.5\mu_B$) in the whole pathway. The electron transfer in the PLS was screened through Bader charge analyses of Fe, substrate, and adsorbed intermediates along with the reaction pathway, as shown in Fig. 5(c). The formation step of

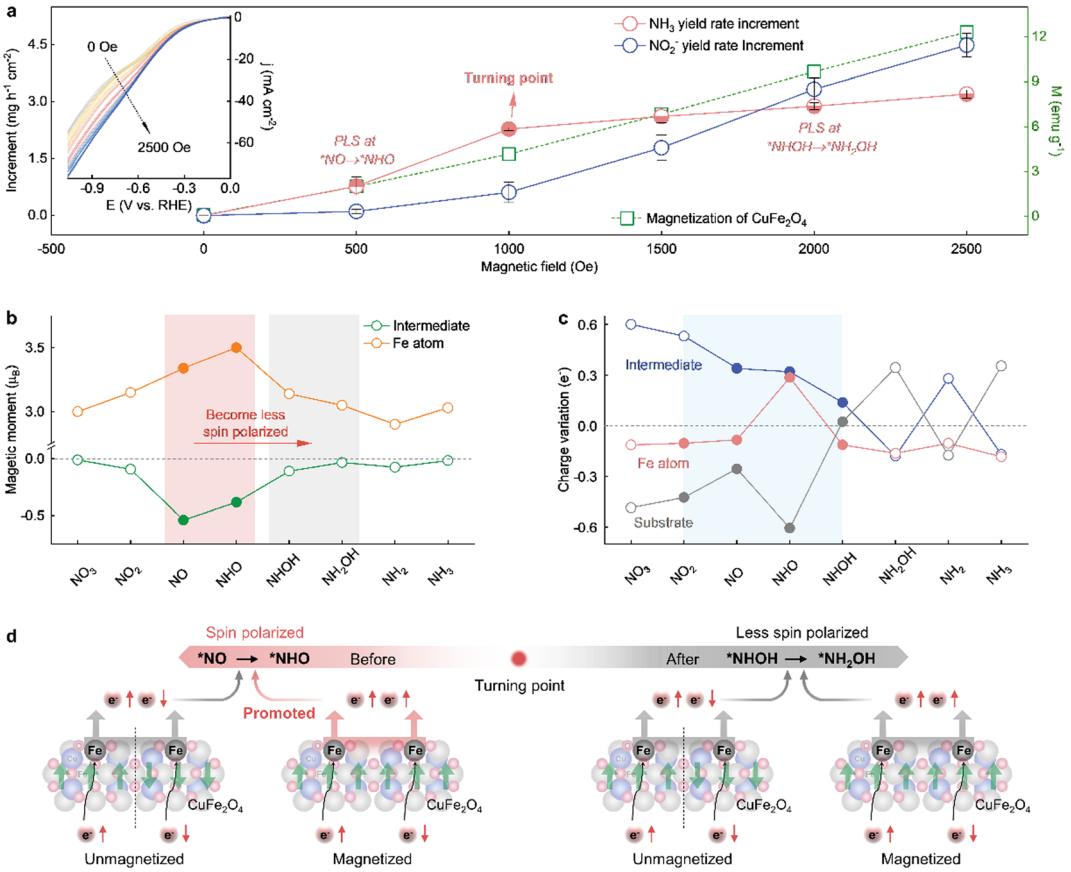

Fig. 5 Linear and non-linear relationships with the net spin of the intermediates. (a) Increment in NH_3 and NO_2^- yield rates at −1.1 V *vs.* RHE under different magnetic field strengths (left axis) and the magnetization of $CuFe_2O_4$ under different magnetic field strengths (right axis, green). The inset in (a) shows the LSV curves of the $CuFe_2O_4$ catalyst at a scan rate of 10 mV s^{-1} in an Ar-saturated electrolyte (0.5 M Na_2SO_4 + 0.1 M $NaNO_3$) under magnetic fields ranging from 0 to 2500 Oe (step: 100 Oe). (b) Magnetic moment of the intermediates, the Fe atom and the substrate involved in NO_3^-RR. (c) Charge variation of the intermediates, the Fe atom and the substrate involved in NO_3^-RR. (d) Schematics of the different promoting effects on *NO → *NHO and *NHOH → *NH_2OH by spin polarization under magnetic fields, which is responsible for the nonlinear spin correlation.

*NHO involves the largest charge transfer (0.606*e*) among all steps, with Fe atoms experiencing the most significant charge increment during this transition. Notably, the charging of Fe sites is accompanied by the discharging of the substrate. This interaction not only highlights a spin-polarized electron transfer mediated by Fe and indicates a plausible source of spin electrons from the ferromagnetic substrate as a spin filter.

The major spin polarization process in the PLS of *NO → *NHO, mediated by Fe in the ferromagnetic catalyst, should maximize the spin-related improvement in NH_3 production. However, when the step of *NO → *NHO is significantly optimized by magnetization, it may no longer be the limiting step for NH_3 production. The steps of *NO → *NHO and *NHOH → *NH_2OH show a close energetic barrier of 0.474 and 0.423 eV, respectively. However, according to the analysis of magnetic moments (Fig. 5(b)), the step of *NHOH → *NH_2OH is much less spin polarized compared to the step of *NO → *NHO. Upon increasing the strength of the magnetic field, more optimization by magnetization is expected for the step of *NO → *NHO compared to *NHOH → *NH_2OH (Fig. 5(d)). When the improvement reaches a critical point, the limiting step may be shifted to the *NHOH → *NH_2OH. Afterward, the NH_3 production rate could be less sensitive to the increasing spin polarization, where a critical turning point makes the non-linear correlation between NH_3 yield rate increment and magnetic field strength. In contrast, NO_2^- production is determined only by the step of *NO_3 → *NO_2, which maintains a linear correlation with the following.

Conclusion

We demonstrated the critical role of spin polarization in altering the limiting step and optimizing the efficiency of NO_3^-RR under magnetic fields. The Cu substitution in Fe_3O_4 contributes to a higher intrinsic NO_3^-RR activity and elevated magnetic coercivity. The highest NO_3^-RR activity has been achieved on magnetic $CuFe_2O_4$ after magnetization. Theoretical studies have revealed a spin correlation specific to Fe 3d orbitals near the Fermi level before and after the NO_3^- adsorption on the Fe site of $CuFe_2O_4$, which facilitates the spin-related π interactions with reaction intermediates and leads to

significant magnetic moments. The highest magnetic moments of the intermediates were identified for the step of *NO → *NHO, which is the primary limiting step. However, as it is optimized by magnetization, the limiting step is shifted to the step of *NHOH → *NH_2OH, which is less spin polarized, for which the reaction kinetics is less responsive to the magnetic field. Therefore, a non-linear correlation to spin polarization of $CuFe_2O_4$ has been found for NH_3 production. In contrast, NO_3^-RR to produce NO_2^- shows linear correlation to spin polarization due to unchangeable PLS.

The linear and non-linear correlations highlight the importance of specifying the spin effects to intermediates with varied magnetic nature. From a practical perspective, linear correlations offer predictable scalability, making it easier to improve catalytic activity with increasing magnetic field strength. However, non-linear correlation indicates that simply increasing spin polarization may not be applicable for optimizing every elemental step, which makes spin engineering for catalysts complicated but scientifically interesting. This study revealed the complicated enhancement of NO_3^-RR activity under magnetic field conditions. It further provided new fundamental insights into the role of spin polarization in each elemental step of NO_3^-RR. This work inspires interest in investigating more reactions that contain complicated intermediates and steps that can be tuned through a spin effect.

Methods

Reagents and materials used

All chemicals used in this study were of analytical grade and were sourced from commercial suppliers. No further purification was conducted before their use.

Preparation of $CuFe_2O_4$

$CuFe_2O_4$ spinel oxides were prepared using a conventional sol–gel method, as described elsewhere.[40] Iron nitrate nonahydrate ($Fe(NO_3)_3{\cdot}9H_2O$) and Copper acetate monohydrate ($Cu(CH_3COO)_2{\cdot}H_2O$) were mixed in a 2 : 1 molar ratio and then dissolved in 60 mL of deionized water. Citric acid, ethylene diamine tetraacetic acid and ammonium hydroxide were added to the solution, which was stirred at 90 °C for about 2 h until a homogeneous gel was formed. The gel was dried in air at 200 °C for 12 h to obtain black oxide powders. These powders were ground and calcined at 800 °C in air for 6 h to obtain $CuFe_2O_4$ spinel oxides. This synthesis procedure was repeated multiple times and showed good reproducibility.

Material characterizations

Powder X-ray diffraction (XRD) data were recorded using a Bruker D8 diffractometer under Cu-Kα radiation source (λ = 1.5418 Å) at a scanning rate of 2° min^{-1} at ambient temperature. The scanning electron microscopy images and energy-dispersive X-ray spectroscopy (EDS) elemental mapping were performed using a scanning electron microscope (SEM, JEOL JSM7600F). High-resolution transmission electron microscopy (HRTEM) images were obtained on a JEOL JEM-2100 plus microscope at an accelerating voltage of 200 KV. X-ray photoelectron spectroscopy (XPS) equipped with a standard Al Kα X-ray source (PHI-5400 machine) operated at 250 W was employed for surface analysis. Soft X-ray absorption spectroscopy (XAS) at the Cu L-edge, Fe L-edge, and O K-edge was conducted at the Australian Synchrotron, part of ANSTO. The field dependence of magnetization data at room temperature was collected from −14 to +14 kOe using vibrating sample magnetometry (VSM, Lake Shore 7400). Ultraviolet-visible (UV-Vis) absorbance spectra were recorded on a Shimadzu UV-2700 spectrophotometer. *In situ* ATR-FTIR was conducted using a Bruker Vertex 80 instrument with an electrochemical VeeMax III apparatus from PIKE. The operando Raman tests were performed using an i-Raman® Plus 785 H Raman spectrometer with a laser wavelength of 785 nm. Nuclear magnetic resonance (NMR) spectra were performed on a Bruker AV 400-MHz NMR spectrometer.

Electrocatalytic NO_3^-RR measurements

The electrochemical experiments were performed in an H-type cell using a three-electrode setup, consisting of a carbon paper (10 × 10 mm) working electrode (WE) with an effective electrode area of 1.0 cm^2 (one-side loading), a platinum foil (15 × 15 mm) counter electrode (CE), and a saturated calomel reference electrode (RE). A BioLogic SP 150 potentiostat workstation was used to record the electrochemical response. The WE was prepared by the ink-cast method, using a mixture of catalysts and acetylene black carbon in ethyl alcohol with a mass ratio of 5 : 1, then Nafion was added as a binder. The ink was ultrasonicated in an ice bath for 60 min to ensure homogeneity. Finally, a certain volume of ink (51 μL) was dropped onto carbon paper with a loading mass of 255 μg cm^{-2}. All potentials were measured against the SCE without iR correction *versus* the RHE reference scale by E (*vs.* RHE) = E (*vs.* SCE) + 0.0591 × pH + 0.241. For the electrochemical NO_3^- reduction reaction, a 25 mL solution containing 0.5 M Na_2SO_4 and 0.1 M $NaNO_3$ was used as the electrolyte.[2] The electrolyte was distributed to the anode and cathode compartments of the H-cell, separated by a Nafion 117 membrane, with each compartment containing 25 mL of electrolyte. Before the measurement, the electrolyte was purged with argon for 20–25 minutes. The linear sweep voltammetry (LSV) was performed in high-purity argon-saturated 0.5 M Na_2SO_4 with or without 0.1 M $NaNO_3$ at a scan rate of 10 mV s^{-1}. Cyclic voltammetry (CV) tests for the double-layer capacitance (C_{dl}) were conducted in 0.5 M Na_2SO_4 solution in the non-faradaic potential range at scan rates of 10, 20, 40, 60, 80, and 100 mV s^{-1}. The ECSA of the working electrodes was calculated by ECSA = C_{dl}/C_s. Chronoamperometry (CA) tests were carried out at different applied potentials, with high-purity argon continuously supplied to the cathode compartment throughout the experiments. The current density presented in this work is normalized to the geometric surface area.

Determination of ammonia content

The generated ammonia concentration was quantified using UV-Vis spectrophotometry and a modified indophenol blue

method. The measured electrolyte volume was diluted to 1 mL to ensure accurate measurement within the detectable range. Subsequently, 1 mL of a 1 M NaOH solution containing 5 wt% sodium citrate and 5 wt% salicylic acid was added to the diluted sample. Next, 0.5 mL of 0.05 M NaClO solution and 0.1 mL of 1.0 wt% sodium nitroferricyanide solution. Next, the resulting indophenol blue solution's absorption spectrum was then recorded using a UV-Vis spectrophotometer (UV-2700) at 655 nm. Finally, the ammonia concentration was calculated based on the absorbance data from the standard ammonium chloride calibration curve.

Calculation of ammonia yield rate and FE

$$\mathrm{NH_3\ yield\ rate\ (\mu g\ h^{-1}\ cm^{-2})} = (c_{\mathrm{NH_3}} \times V)/(t \times S)$$

$$\mathrm{FE_{NH_3}} = (n \times F \times c_{\mathrm{NH_3}} \times V)/(M \times Q) \times 100\%$$

where $c_{\mathrm{NH_3}}$ (μg $\mathrm{mL^{-1}}$) is the measured ammonia concentration, V (mL) is the electrolyte volume in the cathodic compartment, t (h) is the electrochemical reduction time, S is the geometric surface area of WE, n is the number of electrons transferred (n = 8), F is the Faraday constant (96 485 C $\mathrm{mol^{-1}}$), M is the relative molecular mass of $\mathrm{NH_3}$ and Q (C) is the total charge of applied electricity.

Computational methods

Spin-polarized density functional theory (DFT) calculations were carried out using the Vienna *ab initio* simulation package (VASP).[53] The projector-augmented plane-wave method was applied to describe the ion-electron interaction[54] and the generalized gradient approximation within the Perdew–Burke–Ernzerhof functional was used to describe the exchange-correlation interaction.[55] A low-index (110) surface was used to model the adsorption of the intermediates on the spinel $\mathrm{CuFe_2O_4}$ surface, and a 1 × 2 supercell was constructed. The cut-off energy was set as 500 eV, and the systems were optimized until the energy and force were less than 10^{-5} eV and 0.01 eV $\mathrm{Å^{-1}}$. GGA+U calculations were performed using the model proposed by Dudarev *et al.*, with U_{eff} (=Coulomb U − exchange J) values of 4 eV and 5 eV for Fe and Cu, respectively. The Monkhorst–Pack k-point grids were set as 3 × 2 × 1. During the structural optimization, the top two layers and the intermediates were allowed to fully relax while the bottom layers were kept fixed. A vacuum layer larger than 20 Å in the z-direction is employed to prevent the interaction between slabs. Grimme's D3 method is used to consider the van der Waals (vdW) interactions.[56]

The overall reaction pathway can be described by the following sequence of elementary steps:

$$* + \mathrm{NO_3^-} \rightarrow *\mathrm{NO_3} + \mathrm{e^-}$$

$$*\mathrm{NO_3} + 2\mathrm{H^+} + 2\mathrm{e^-} \rightarrow *\mathrm{NO_2} + \mathrm{H_2O}$$

$$*\mathrm{NO_2} + 2\mathrm{H^+} + 2\mathrm{e^-} \rightarrow *\mathrm{NO} + \mathrm{H_2O}$$

$$*\mathrm{NO} + \mathrm{H^+} + \mathrm{e^-} \rightarrow *\mathrm{NHO}$$

$$*\mathrm{NHO} + \mathrm{H^+} + \mathrm{e^-} \rightarrow *\mathrm{NHOH}$$

$$*\mathrm{NHOH} + \mathrm{H^+} + \mathrm{e^-} \rightarrow *\mathrm{NH_2OH}$$

$$*\mathrm{NH_2OH} + \mathrm{H^+} + \mathrm{e^-} \rightarrow *\mathrm{NH_2} + \mathrm{H_2O}$$

$$*\mathrm{NH_2} + \mathrm{H^+} + \mathrm{e^-} \rightarrow *\mathrm{NH_3}$$

where * denotes the catalytically active site.

The corresponding Gibbs free energy change for each step is calculated using the following equation:

$$\Delta G = \Delta E + \Delta E_{\mathrm{ZPE}} - T\Delta S$$

where ΔE is the total energy difference before and after the intermediate adsorption, ΔE_{ZPE} is the difference in zero-point energy, and ΔS is the entropy change. The zero-point energies and entropies of both free molecules and adsorbed species were obtained from vibrational frequency calculations. To describe the charged $\mathrm{NO_3^-}$ species as a reference, neutral $\mathrm{HNO_3}$ in the gas phase was used as a reference, and the energy of $\mathrm{NO_3^-}$ was derived *via* a thermodynamic cycle, avoiding challenges in modeling charged systems using periodic DFT.[57]

Author contributions

D. S., T. W., and Z. X. conceived the idea and designed the experiment. D. S. was responsible for catalyst design. D. S. and X. C. performed electrochemical measurements and all authors contributed to the data analysis. Q. W. conducted the DFT studies. C. D. conducted the *in situ* ATR-FTIR and operando Raman tests. S. Z. conducted the magnetic hysteresis loop. F. M. conducted the isotope-labeling test and analysis. Y. Z. and P. S. performed the HRTEM characterizations. X. L., S. Z., and T. W. performed the soft XAS measurement and analyses. Y. Z., D. S., and T. W. prepared the figures. D. S., T. W., Y. Z., and Z. X. prepared the manuscript with contributions from all authors.

Conflicts of interest

There are no conflicts to declare.

Data availability

All data supporting the findings of this study are available within the article and its ESI† file or from the authors upon reasonable request.

Acknowledgements

This work was financially supported by the Singapore Ministry of Education Tier 2 Grant (MOE-T2EP10220-0001). C. Dai acknowledges the support by the National Research Foundation, Prime Minister's Office, Singapore, under its Campus for

Research Excellence and Technological Enterprise (CREATE) program. The authors thank for the XAS measurements from the Soft X-ray Spectroscopy beamline, the Australian Synchrotron (AS, Australia), part of ANSTO.

References

1 J. Huang, B. Hu, J. Meng, T. Meng, W. Liu, Y. Guan, L. Jin and X. Zhang, *Energy Environ. Sci.*, 2024, **17**, 1007–1045.
2 N. T. Suen, S. F. Hung, Q. Quan, N. Zhang, Y. J. Xu and H. M. Chen, *Chem. Soc. Rev.*, 2017, **46**, 337–365.
3 S. Jin, J. M. Kevin, A. G. Hubert, B. G. John and S.-H. Yang, *Science*, 2011, **334**, 1383–1385.
4 M. G. Kibria, J. P. Edwards, C. M. Gabardo, C. T. Dinh, A. Seifitokaldani, D. Sinton and E. H. Sargent, *Adv. Mater.*, 2019, **31**, e1807166.
5 G. Zhang, B. Li, Y. Shi, Q. Zhou, W.-J. Fu, G. Zhou, J. Ma, S. Yin, W. Yuan, S. Miao, Q. Ji, J. Qu and H. Liu, *Nat. Sustain.*, 2024, **7**, 1251–1263.
6 F.-Y. Chen, A. Elgazzar, S. Pecaut, C. Qiu, Y. Feng, S. Ashokkumar, Z. Yu, C. Sellers, S. Hao, P. Zhu and H. Wang, *Nat. Catal.*, 2024, **7**, 1032–1043.
7 J. K. Norskov, F. Abild-Pedersen, F. Studt and T. Bligaard, *Proc. Natl. Acad. Sci. U. S. A.*, 2011, **108**, 937–943.
8 F. Calle-Vallejo, N. G. Inoglu, H.-Y. Su, J. I. Martínez, I. C. Man, M. T. M. Koper, J. R. Kitchin and J. Rossmeisl, *Chem. Sci.*, 2013, **4**, 1245–1249.
9 A. Grimaud, K. J. May, C. E. Carlton, Y. L. Lee, M. Risch, W. T. Hong, J. Zhou and Y. Shao-Horn, *Nat. Commun.*, 2013, **4**, 2439.
10 J. Suntivich, W. T. Hong, Y.-L. Lee, J. M. Rondinelli, W. Yang, J. B. Goodenough, B. Dabrowski, J. W. Freeland and Y. Shao-Horn, *J. Phys. Chem. C*, 2014, **118**, 1856–1863.
11 W. T. Hong, R. E. Welsch and Y. Shao-Horn, *J. Phys. Chem. C*, 2015, **120**, 78–86.
12 M. T. M. Koper, *J. Electroanal. Chem.*, 2011, **660**, 254–260.
13 M. T. M. Koper, *Chem. Sci.*, 2013, **4**, 2710–2723.
14 J. Gracia, *Phys. Chem. Chem. Phys.*, 2017, **19**, 20451–20456.
15 J. Gracia, R. Sharpe and J. Munarriz, *J. Catal.*, 2018, **361**, 331–338.
16 J. Munarriz, V. Polo and J. Gracia, *Chemphyschem*, 2018, **19**, 2843–2847.
17 X. Ren, T. Wu, Y. Sun, Y. Li, G. Xian, X. Liu, C. Shen, J. Gracia, H. J. Gao, H. Yang and Z. J. Xu, *Nat. Commun.*, 2021, **12**, 2608.
18 T. Wu, X. Ren, Y. Sun, S. Sun, G. Xian, G. G. Scherer, A. C. Fisher, D. Mandler, J. W. Ager, A. Grimaud, J. Wang, C. Shen, H. Yang, J. Gracia, H. J. Gao and Z. J. Xu, *Nat. Commun.*, 2021, **12**, 3634.
19 X. Ren, T. Wu, Z. Gong, L. Pan, J. Meng, H. Yang, F. B. Dagbjartsdottir, A. Fisher, H. J. Gao and Z. J. Xu, *Nat. Commun.*, 2023, **14**, 2482.
20 J. Gracia, *Phys. Chem. Chem. Phys.*, 2017, **19**, 20451–20456.
21 J. Gracia, *J. Phys. Chem. C*, 2019, **123**, 9967–9972.
22 W. Mtangi, V. Kiran, C. Fontanesi and R. Naaman, *J. Phys. Chem. Lett.*, 2015, **6**, 4916–4922.
23 Z. Chen, X. Li, H. Ma, Y. Zhang, J. Peng, T. Ma, Z. Cheng, J. Gracia, Y. Sun and Z. J. Xu, *Natl. Sci. Rev.*, 2024, **11**, nwae314.
24 W. Zhang, J. Ai, T. Ouyang, L. Yu, A. Liu, L. Han, Y. Duan, C. Tian, C. Chu, Y. Ma, S. Che and Y. Fang, *J. Am. Chem. Soc.*, 2024, **146**, 28214–28221.
25 J. Dai, Y. Tong, L. Zhao, Z. Hu, C. T. Chen, C. Y. Kuo, G. Zhan, J. Wang, X. Zou, Q. Zheng, W. Hou, R. Wang, K. Wang, R. Zhao, X. K. Gu, Y. Yao and L. Zhang, *Nat. Commun.*, 2024, **15**, 88.
26 K. Zhang, A. Cao, L. H. Wandall, J. Vernieres, J. Kibsgaard, J. K. Nørskov and I. Chorkendorff, *Science*, 2024, **383**, 1357–1363.
27 Y. Wang, A. Xu, Z. Wang, L. Huang, J. Li, F. Li, J. Wicks, M. Luo, D. H. Nam, C. S. Tan, Y. Ding, J. Wu, Y. Lum, C. T. Dinh, D. Sinton, G. Zheng and E. H. Sargent, *J. Am. Chem. Soc.*, 2020, **142**, 5702–5708.
28 Q. Hu, Q. Huo, S. Qi, X. Deng, J. Zhuang, J. Yu, X. Li, W. Zhou, M. Lv, X. Chen, X. Wang, C. Feng, H. Yang and C. He, *Adv. Mater.*, 2023, **36**, 2311375.
29 K. Liu, H. Li, M. Xie, P. Wang, Z. Jin, Y. Liu, M. Zhou, P. Li and G. Yu, *J. Am. Chem. Soc.*, 2024, **146**, 7779–7790.
30 S. Han, H. Li, T. Li, F. Chen, R. Yang, Y. Yu and B. Zhang, *Nat. Catal.*, 2023, **6**, 402–414.
31 Y. Wang, C. Wang, M. Li, Y. Yu and B. Zhang, *Chem. Soc. Rev.*, 2021, **50**, 6720–6733.
32 J. Crawford, H. Yin, A. Du and A. P. O'Mullane, *Angew. Chem., Int. Ed.*, 2022, **61**, e202201604.
33 J. Cai, Y. Wei, A. Cao, J. Huang, Z. Jiang, S. Lu and S.-Q. Zang, *Appl. Catal., B*, 2022, **316**, 121683.
34 Q. Gao, H. S. Pillai, Y. Huang, S. Liu, Q. Mu, X. Han, Z. Yan, H. Zhou, Q. He, H. Xin and H. Zhu, *Nat. Commun.*, 2022, **13**, 2338.
35 J.-Y. Fang, Q.-Z. Zheng, Y.-Y. Lou, K.-M. Zhao, S.-N. Hu, G. Li, O. Akdim, X.-Y. Huang and S.-G. Sun, *Nat. Commun.*, 2022, **13**, 7899.
36 J. Wang, K. Zhao, Y. Yao, F. Xue, F. Lu, W. Yan, F. Yuan and X. Wang, *Nat. Commun.*, 2025, **16**, 1129.
37 X. He, F. Yang, Q. Hu, J. Yin and J. Zhang, *Crystals*, 2023, **13**, 1640.
38 W. Chen, X. Yang, Z. Chen, Z. Ou, J. Hu, Y. Xu, Y. Li, X. Ren, S. Ye, J. Qiu, J. Liu and Q. Zhang, *Adv. Funct. Mater.*, 2023, **33**, 2300512.
39 C. Liu, X.-C. Zhou, G. Li, J. Su, L. Tang, Q. Liu, X. Han, S. Lv, Z. Mu, Y. Sun, S. Yuan, F. Gao, J.-L. Zuo, S. Li and M. Ding, *Sci. Adv.*, 2025, **11**, eadq3554.
40 T. Wu, S. Sun, J. Song, S. Xi, Y. Du, B. Chen, W. A. Sasangka, H. Liao, C. L. Gan, G. G. Scherer, L. Zeng, H. Wang, H. Li, A. Grimaud and Z. J. Xu, *Nat. Catal.*, 2019, **2**, 763–772.
41 K. Verma, A. Kumar and D. Varshney, *Curr. Appl. Phys.*, 2013, **13**, 467–473.
42 R. Zhang, M. Liu, L. Lu, S.-B. Mi, C.-L. Jia and H. Wang, *RSC Adv.*, 2016, **6**, 100108.
43 V. N. Popok, S. M. Novikov, Y. Y. Lebedinskij, A. M. Markeev, A. A. Andreev, I. N. Trunkin, A. V. Arsenin and V. S. Volkov, *Plasmonics*, 2020, **16**, 333–340.
44 M. Swadzba-Kwasny, L. Chancelier, S. Ng, H. G. Manyar, C. Hardacre and P. Nockemann, *Dalton Trans.*, 2012, **41**, 219–227.

45 Y. Wang, W. Zhou, R. Jia, Y. Yu and B. Zhang, *Angew. Chem., Int. Ed.*, 2020, **59**, 5350–5354.
46 M. Nasir, N. Patra, D. K. Shukla, D. Bhattacharya, S. Kumar, D. M. Phase, S. N. Jha, S. Biring, P. M. Shirage and S. Sen, *RSC Adv.*, 2016, **6**, 103571.
47 J. Yang, T. Regier, J. J. Dynes, J. Wang, J. Shi, D. Peak, Y. Zhao, T. Hu, Y. Chen and J. S. Tse, *Anal. Chem.*, 2011, **83**, 7856–7862.
48 Y. Li, C. Wang, L. Yang, W. Ge, J. Shen, Y. Zhu and C. Li, *Adv. Energy Mater.*, 2023, **14**, 2303863.
49 M. A. Larrubia, G. Ramis and G. Busca, *Appl. Catal., B*, 2001, **30**, 101–110.
50 V. Rosca, G. L. Beltramo and M. T. M. Koper, *J. Electroanal. Chem.*, 2004, **566**, 53–62.
51 Z. Huang, B. Yang, Y. Zhou, W. Luo, G. Chen, M. Liu, X. Liu, R. Ma and N. Zhang, *ACS Nano*, 2023, **17**, 25091–25100.
52 Q. Hu, K. Yang, O. Peng, M. Li, L. Ma, S. Huang, Y. Du, Z. X. Xu, Q. Wang, Z. Chen, M. Yang and K. P. Loh, *J. Am. Chem. Soc.*, 2024, **146**, 668–676.
53 G. Kresse and J. Furthmüller, *Phys. Rev. B: Condens. Matter Mater. Phys.*, 1996, **54**, 11169–11186.
54 P. E. Blochl, *Phys. Rev. B: Condens. Matter Mater. Phys.*, 1994, **50**, 17953–17979.
55 G. Kresse and D. Joubert, *Phys. Rev. B: Condens. Matter Mater. Phys.*, 1999, **59**, 1758–1775.
56 S. Grimme, *J. Comput. Chem.*, 2006, **27**, 1787–1799.
57 S. Guo, K. Heck, S. Kasiraju, H. Qian, Z. Zhao, L. C. Grabow, J. T. Miller and M. S. Wong, *ACS Catal.*, 2017, **8**, 503–515.